INTERNATIONAL JOURNAL FOR NUMERICAL METHODS IN FLUIDS
Int. J. Numer. Meth. Fluids **28**: 1281–1302 (1998)

LARGE EDDY SIMULATION OF THE SUBCRITICAL FLOW PAST A CIRCULAR CYLINDER: NUMERICAL AND MODELING ASPECTS

M. BREUER*

Lehrstuhl für Strömungsmechanik, Universität Erlangen-Nürnberg, Cauerstr. 4, D-91058 Erlangen, Germany

SUMMARY

The turbulent flow past a circular cylinder ($Re = 3900$) was computed by large eddy simulation (LES). The objective was not to investigate the physical phenomena of this flow in detail but to study numerical and modeling aspects which influence the quality of LES solutions. Concerning the numerical method, the most important component is the discretization of the non-linear convective fluxes. Five different schemes were investigated. Also, the influence of different grid resolutions was examined. Two aspects play an important role on the modeling side, namely the near-wall model and the subgrid scale model. Owing to the restriction to low Reynolds numbers in this study, no-slip boundary conditions were used at solid walls. Therefore, only the second aspect was taken into account. Two different subgrid scale models were applied. Additionally, LES computations without any subgrid scale modeling were carried out in order to prove the performance of the models. The results were evaluated by comparison with available experimental data. © 1998 John Wiley & Sons, Ltd.

KEY WORDS: large eddy simulation; turbulent flow; circular cylinder; accuracy; finite volume method; subgrid scale model

1. INTRODUCTION

In general, turbulent flows past bluff bodies, including complex phenomena such as separation, reattachment or vortex shedding, are very complicated. An appropriate description using Reynolds-averaged Navier–Stokes equations combined with statistical turbulence models is difficult to achieve. In contrast to statistical turbulence models, direct numerical simulations (DNS) require no extra assumptions but will not be applicable to engineering flows in the near future. The concept of large eddy simulation (LES) offers a suitable method for solving such flow problems. The large eddies in LES which depend strongly on the special flow configuration and its boundary conditions are resolved numerically, whereas only the fine scale turbulence has to be modeled by a subgrid scale model.

Before LES can be used for applications of practical relevance the influences on the quality of LES solutions must be understood. This includes numerical aspects such as discretization schemes or resolution requirements, and modeling aspects such as subgrid scale models or near-wall models. Owing to extremely long computation times, detailed studies on this important topic are rare, especially for test cases which are geometrically and physically more challenging than standard LES test cases, such as plane channel flow.

* Correspondence to: Lehrstuhl für Strömungsmechanik, Universität Erlangen-Nürnberg, Cauerstr. 4, D-91058 Erlangen, Germany.

CCC 0271–2091/98/191281–22$17.50

Received August 1997
Revised December 1997

There have been attempts to distribute the load among different groups by organizing workshops on LES for specified test cases. One of these was the 'Workshop on LES of Flows Past Bluff Bodies' at Tegernsee, June 1995. The results have been published by Rodi *et al.* [1] Despite the large number of contributions it was difficult to draw any concrete conclusions. Different groups applied different numerical methods on grids with varying resolutions, using different subgrid scale models and wall boundary conditions. Much of what was learned in terms of how the various factors affect the results was derived from those cases in which a single group made multiple simulations that differed in just one factor. A similar workshop was held in Grenoble, September 1996. At this '2nd ERCOFTAC Workshop on Direct and Large Eddy Simulation' [2] one of the test cases of the Tegernsee Workshop was tackled once more. Again, the most valuable results were those from participants who performed systematic and detailed studies varying only one parameter per simulation.

The objective of the work reported here was to continue such efforts in order to learn more about LES and the important factors affecting the quality of the solution. In contrast to the test cases of the LES workshop at Tegernsee (flow past a square cylinder and flow past a cubic obstacle), which could be tackled using Cartesian grids, a geometrically and physically more complex flow problem is considered, namely the flow past a long, circular cylinder at a subcritical Reynolds number of $Re = 3900$. In contrast to its square counterpart, this flow configuration requires curvilinear body-fitted (or unstructured) grids. There is a lack of experience concerning the applicability and properties of such grids using LES, because most of the previous investigations on simple test cases have been based either on Cartesian grids (finite difference and finite volume methods) or spectral methods. However, in order to compute practically relevant flow problems, such as the flow around a complete automobile or aircraft by the method of LES, curvilinear body-fitted grids are essential. Before LES can be applied to such complicated flows, extensive tests must be carried out on simpler configurations, such as circular cylinder flow. Vortex shedding past a circular cylinder is also physically more challenging than the square cylinder test case because the separation point on the surface of the cylinder is not fixed by the geometry. These characteristics of the circular cylinder flow, combined with the enormous number of experimental studies on the vortex dynamics of cylinder wakes (see, e.g. Reference [3]), reveals this flow to be an excellent test case for the intended investigations on LES of bluff body aerodynamics.

The following section starts with some general remarks on the numerical simulation process and the errors which must be taken into account. Then the governing equations for LES are given and two different subgrid scale models used in the present study are described. The subsequent section presents the method of solution, aiming especially at the spatial discretization of the non-linear convective fluxes. The details of the test case are given in the next section. Finally, the results are presented and discussed. As mentioned above, the simulations were evaluated with the intention of learning more about the numerical and modeling aspects influencing the quality of LES results.

2. NUMERICAL SIMULATION PROCESS AND ACCURACY

The entire procedure of a numerical simulation is illustrated schematically in Figure 1. The starting point of any simulation is the physical system which should be described. In the context of LES this is, of course, represented by a turbulent flow. First, a mathematical model for the behavior of the physical system has to be defined. This step yields the first of three kinds of systematic errors involved in the simulation procedure. The *modeling error* describes

the difference between the behavior of the physical system and the exact solution of the mathematical model. As well as the governing equations, the filter formulation, the model for the subgrid scale (SGS) stresses and the approximations of the boundary conditions determine the size of this type of error in an LES. After selecting a mathematical model, the basic equations must be discretized because generally no analytical solutions exist for complex physical systems. This introduces the second kind of error, called *discretization error*, defined as the difference between the exact solution of the mathematical model and the exact solution of the discretized equations. In computational fluid dynamics (CFD), the size of this error can be reduced by an appropriate discretization method and a sufficiently fine resolution. Finally, the third type of error, called *convergence error*, arises out of the difference between the iterative and the exact solution of the discretized equations. It depends on the solver applied and the convergence criteria chosen.

These different types of errors should be clearly distinguished, even though in general they are completely mixed up in the discrete solution of the physical problem. Nevertheless, one should be aware of these errors strongly influencing the quality of any CFD simulation, not only of LES. In this work the investigations were restricted to four aspects, namely the governing equations (2D versus 3D), the subgrid scale model, the discretization scheme and the resolution.

3. GOVERNING EQUATIONS

A fascinating property of the Navier–Stokes equations is their capability to describe even the most complex turbulent flow. It is well-known that, in principle, no turbulence modeling is necessary. DNS, however, is totally impracticable for high Reynolds number flow problems for the foreseeable future. Statistical turbulence models based on the Reynolds-averaged equations have been developed for decades with limited success, especially for highly complex turbulent

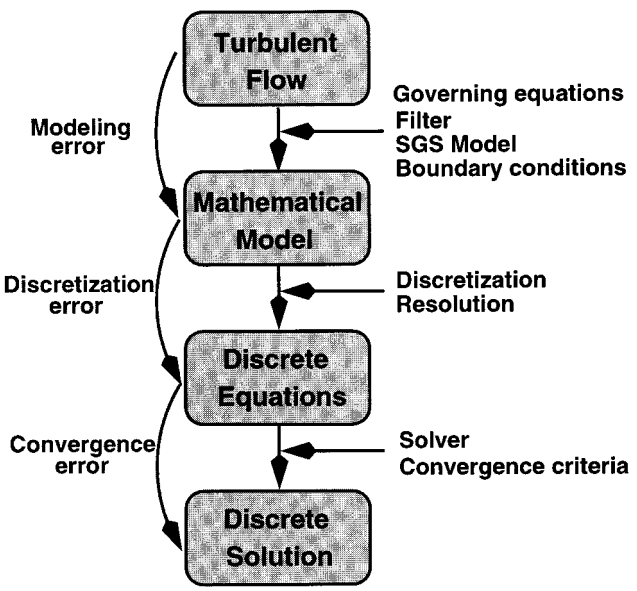

Figure 1. Numerical and modeling aspects in LES, different kinds of errors involved.

flows such as those occurring in bluff body aerodynamics. This is due to the fact that these approaches have to describe the whole spectrum of turbulent eddies. The concept of LES overcomes this drawback. Only the influence of the small eddies has to be modeled by a subgrid scale model, whereas the large energy-carrying eddies are computed directly. Small eddies are more universal, random, homogeneous and isotropic, which simplifies the development of appropriate models.

In order to separate the large- and small-scale motions, the three-dimensional, time dependent Navier–Stokes equations are filtered. In the present study a box filter is applied as a filter kernel and an incompressible fluid is assumed. The governing equations are given by (see, e.g. Reference [4])

$$\frac{\partial \bar{u}_i}{\partial x_i} = 0, \tag{1}$$

$$\frac{\partial \bar{u}_i}{\partial t} + \frac{\partial}{\partial x_j}(\bar{u}_i \bar{u}_j) = -\frac{\partial \bar{p}}{\partial x_i} + \frac{\partial}{\partial x_j}\left[\frac{1}{Re}\left(\frac{\partial \bar{u}_i}{\partial x_j} + \frac{\partial \bar{u}_j}{\partial x_i}\right)\right] - \frac{\partial \tau_{ij}}{\partial x_j}, \tag{2}$$

$$\tau_{ij} = \overline{u_i u_j} - \overline{u_i}\,\overline{u_j}, \tag{3}$$

where $\bar{u}_i$ is the velocity component of the resolved scales, $\bar{p}$ is the corresponding pressure and Re is the Reynolds number. The filtering procedure provides the governing equations for the resolvable scales of the flow field. Although the continuity equation (1) of the resolved quantities is equal to the original unfiltered one, the filtered momentum equation (2) includes an additional term for the non-resolvable subgrid scale stresses τ_{ij}, which results from filtering the non-linear convective fluxes. τ_{ij} describes the influence of the small-scale structures on the larger eddies. Only this effect has to be modeled by a subgrid scale model. For simplicity, Equations (1) and (2) are given here in Cartesian co-ordinates. However, as pointed out above, the computation of flows in complex geometries requires either unstructured or curvilinear boundary-fitted (structured) grids which, in general, are non-orthogonal. The application of a co-ordinate transformation allows the governing equations to be easily rewritten for a general system of co-ordinates, as used in the computer code.

4. SUBGRID SCALE MODELS

4.1. Smagorinsky model

In principle, the LES concept leads to a closure problem similar to that obtained by the Reynolds-averaged approach. Therefore, a similar classification of turbulence models starting with zero-equation models and ending up with Reynolds stress models is possible. However, the non-resolvable small-scale turbulence in a LES is much less problem-dependent than the large-scale turbulence, so that the subgrid scale turbulence can be represented by relatively simple models, e.g. zero-equation eddy-viscosity models. The well-known Smagorinsky model [5] is most often used and, like other eddy viscosity models for LES, it is based on Boussinesq's approach, assuming that in analogy to the viscous stresses in laminar flows, the turbulent stresses are proportional to the mean velocity gradients, or more general to the large-scale strain rate tensor $\bar{S}_{ij}$:

$$\tau_{ij}^{a} = \tau_{ij} - \delta_{ij}\tau_{kk}/3 = -2\nu_T \bar{S}_{ij}, \tag{4}$$

where τ_{ij}^{a} is the anisotropic (traceless) part of the subgrid scale Reynolds stresses τ_{ij}, and δ_{ij} is the Kronecker delta. The trace of the stress tensor is usually added to the filtered pressure $\bar{p}$, resulting in the new pressure P

$$P = \bar{p} + \tau_{kk}/3. \tag{5}$$

The eddy viscosity ν_T itself is a function of the strain rate tensor $\bar{S}_{ij}$ and the subgrid length l, as

$$\nu_T = l^2|\bar{S}_{ij}|, \tag{6}$$

$$\bar{S}_{ij} = \frac{1}{2}\left(\frac{\partial \bar{u}_i}{\partial x_j} + \frac{\partial \bar{u}_j}{\partial x_i}\right), \tag{7}$$

$$|\bar{S}_{ij}| = \sqrt{2\bar{S}_{ij}\bar{S}_{ij}}. \tag{8}$$

The subgrid length l is assumed to be proportional to the filter width $\bar{\Delta}$:

$$l = C_s\bar{\Delta} = C_s(\Delta x\ \Delta y\ \Delta z)^{1/3}, \tag{9}$$

where C_s is a free parameter called the Smagorinsky constant. The filter width $\bar{\Delta}$ is correlated with a typical grid spacing given by the cube root of the cell volume. Taking into account the reduction of the subgrid length l near solid walls, the length scale is usually multiplied by a Van Driest damping function, as

$$l = C_s\bar{\Delta}\,[1 - \exp(-y^+/25)^3]^{0.5}. \tag{10}$$

Although theoretical values of $C_s \approx 0.16$ for homogeneous, isotropic turbulence can be found in the literature, smaller values are usually applied in LES computations of non-homogeneous and non-isotropic flows leading to improved results. All computations in the present work were carried out with a Smagorinsky constant of $C_s = 0.1$, which is a typical value for practical applications of the Smagorinsky model.

4.2. Dynamic model

One of the major drawbacks of the Smagorinsky model is that the Smagorinsky constant C_s was found to depend on the flow problem considered. Second, in an inhomogeneous flow, the optimum choice for C_s may be different for different regions in the flow. The Smagorinsky model also needs additional assumptions to describe flows undergoing transition or near solid walls (see Equation (10)). The dynamic model, originally proposed by Germano *et al.* [6], eliminates some of these disadvantages by calculating a 'Smagorinsky constant' as a function of time and position. Based on the local equilibrium approach (production = dissipation), the eddy viscosity is again evaluated from Equation (6). In contrast to the Smagorinsky model, however, $C_s^2 = C$ is no longer a constant, but a local, time-dependent variable. The dynamic approach represents a method for determining this unknown variable C from the information already contained in the resolved velocity field. Germano *et al.* [6] devised a systematic procedure for computing turbulent flows by LES, without the necessity for prior experience in order to properly adjust the Smagorinsky constant. The basic formalism behind the method is summarized briefly. First a test filter which has a larger filter width than the original filter ($\tilde{\bar{\Delta}} > \bar{\Delta}$) is introduced. Applying the test filter to the filtered Navier–Stokes equation (2) gives the subgrid scale stress tensor T_{ij} similar to τ_{ij}:

$$T_{ij} = \widetilde{\bar{u}_i\bar{u}_j} - \tilde{\bar{u}}_i\tilde{\bar{u}}_j. \tag{11}$$

The resolvable part $\mathscr{L}_{ij}$ is defined by

$$\mathscr{L}_{ij} = \widetilde{\bar{u}_i \bar{u}_j} - \tilde{\bar{u}}_i \tilde{\bar{u}}_j. \tag{12}$$

The two stress tensors τ_{ij} and T_{ij} are related by the Germano identity

$$\mathscr{L}_{ij} = T_{ij} - \tilde{\tau}_{ij}. \tag{13}$$

Assuming that the same functional form (Smagorinsky model) and parameter C_s can be used to model the anisotropic parts of both τ_{ij} and T_{ij}, yields

$$\tau_{ij}^{a} = -2(C_s\bar{\Delta})^2 |\bar{S}_{ij}| \bar{S}_{ij}, \tag{14}$$

$$T_{ij}^{a} = -2(C_s\tilde{\bar{\Delta}})^2 |\tilde{\bar{S}}_{ij}| \tilde{\bar{S}}_{ij}, \tag{15}$$

where $\tilde{\bar{S}}_{ij}$ is the strain rate tensor of the test-filtered velocity field, defined as

$$\tilde{\bar{S}}_{ij} = \frac{1}{2}\left(\frac{\partial \tilde{\bar{u}}_i}{\partial x_j} + \frac{\partial \tilde{\bar{u}}_j}{\partial x_i}\right). \tag{16}$$

Note that the idea of the dynamic approach is not restricted to the use of the Smagorinsky model as a so-called base model. In principle, other models (e.g. the Bardina model [7]) can be used within the dynamic procedure, resulting in an algorithm used to systematically compute the constants of this base model as a function of space and time instead of the Smagorinsky value.

Rearranging Equations (13), (14) and (15) yields

$$\mathscr{L}_{ij} = -2(C_s\bar{\Delta})^2 \left[\frac{\tilde{\bar{\Delta}}^2}{\bar{\Delta}^2} |\tilde{\bar{S}}_{ij}| \tilde{\bar{S}}_{ij} - \widetilde{|\bar{S}_{ij}| \bar{S}_{ij}}\right] = -2(C_s\bar{\Delta})^2 \mathscr{M}_{ij}. \tag{17}$$

Following a suggestion by Lilly [8] a least-squares approach is used to obtain values for $(C_s\bar{\Delta})^2$, leading to

$$C\bar{\Delta}^2 = (C_s\bar{\Delta})^2 = -\frac{1}{2}\frac{\mathscr{L}_{ij}\mathscr{M}_{ij}}{\mathscr{M}_{ij}\mathscr{M}_{ij}}. \tag{18}$$

Tests with this formulation of the dynamic model have shown that, in principle, negative values of C are possible. In practice, however, these are not able to represent the backscatter effect because negative eddy viscosities strongly destabilize the numerical algorithm. Furthermore, C is an instantaneous and local quantity varying very much in space and time. This also leads to numerical instabilities. Different possibilities have been tested to remove this problem. Depending on the flow problem, different kinds of averaging procedures can be applied in the dynamic approach. If the flow is homogeneous in a certain direction, the numerator and denominator of Equation (18) can be averaged with respect to the corresponding direction. For fully inhomogeneous flows, only an averaging procedure in time is applicable. So that the values of C are not restricted to a fully time independent function and to allow variations with low frequencies, a special form of time averaging (low-pass filtering) is chosen, which is well-known as a recursive low-pass digital filter:

$$C_{\text{filtered}}^{(n+1)} = (1-\epsilon)\, C^{n} + \epsilon\, C^{(n+1)}. \tag{19}$$

With a filter parameter of ϵ of the order 10^{-3}, all high-frequency oscillations are damped out and only the low-frequency variations remain. This seems to be better than fully freezing C. In the case of the flow past a circular cylinder, it was necessary to average in the homogeneous direction as well as in time ($\epsilon = 10^{-3}$), in order to obtain a stable solution. Additionally, negative eddy viscosities are clipped.

4.3. No subgrid scale model

Moreover, LES computations were performed without any subgrid scale model in order to investigate the influence of the model on the resolved scales. These simulations were deliberately not called direct numerical simulations because they did not comply with the requirements of DNS. In the author's opinion, a simulation should only be denoted as DNS if the spatial and temporal resolution is fine enough to resolve the smallest scales in a turbulent flow, namely the Kolmogorov length and time scale. Regarding the grids used in the present study (see Table III), this condition was never fulfilled, leading to the notation of 'LES without subgrid scale model'.

5. METHOD OF SOLUTION

5.1. Spatial discretization

The code (**LESOCC** = Large Eddy Simulation On Curvilinear Co-ordinates), which is used to solve the filtered Equations (1) and (2), is based on a 3D finite volume method for arbitrary non-orthogonal, body-fitted grids [9–14]. The finite volume approach uses the integral form of the conservation equations (1) and (2) as its starting point. This can be derived from the differential form by integration over a control volume and by applying the Gauss theorem to transform volume integrals into surface integrals. These surface integrals (= fluxes F) are approximated by the midpoint rule, which is equivalent to the product of the integrand f at the cell face center and the cell face area A:

$$F_{i+1/2} = \int_{A_{i+1/2}} f \cdot \mathrm{d}A \approx f_{i+1/2} \cdot A_{i+1/2}. \tag{20}$$

This approximation is of second-order accuracy in space if the value of f is known at the location $i+\frac{1}{2}$. For a cell-centered (non-staggered) grid arrangement, as used in **LESOCC**, the values of f at the cell faces are not available and must be obtained by interpolation. In order to examine the influence of the interpolation scheme, especially for the non-linear convective fluxes, five different options have been investigated. For simplification these schemes are described here under the assumption of a uniform Cartesian grid and a positive flow direction. Then the approximation for the value at the east cell face is given in Table I.

The HYBRID scheme is a combination of two different approximations. It switches between the upwind differencing scheme (UDS) and the central differencing scheme (CDS-2) depending on the local value of the Peclet number ($Pe = u\Delta x/\nu$). In general, the Peclet number for LES is > 2. Therefore, the leading truncation error term $\mathscr{T}$ of this scheme is proportional to the grid spacing Δx. The HYBRID scheme satisfies the boundedness criterion unconditionally. However, it is known to be numerically diffusive and therefore not well suited for LES. Nevertheless, it is added here for completeness. The CDS-2 scheme linearly interpolates the value at the cell face, which leads to a truncation error term proportional to the square of the grid spacing Δx^2. This scheme has often been used for LES computations. The HLPA scheme (Hybrid Linear/Parabolic Approximation) was proposed by Zhu [15] and combines a second-order upstream-weighted approximation with first-order upwind differencing under the control of a convection boundedness criterion. Zhu claims that HLPA is capable of yielding low diffusive and always bounded solutions. The first property in particular makes this scheme worth investigating in the context of LES. The QUICK scheme, originally proposed by Leonard [16], is a logical improvement of the CDS-2 scheme. Instead of a straight line between

Table I. Overview of all interpolation schemes in **LESOCC**

Convection scheme	Value at cell face: $f_{i+1/2} =$	Order of error $\mathscr{T}$
HYBRID	$\begin{cases} \frac{1}{2}(f_i+f_{i+1}) & : Pe_{i+1/2} \le 2 \\ f_i & : \text{otherwise} \end{cases}$	Δx^2 Δx
CDS-2	$\frac{1}{2}(f_i+f_{i+1})$	Δx^2
HLPA	$f_i+\gamma(f_{i+1}-f_i)\left(\frac{f_i-f_{i-1}}{f_{i+1}-f_{i-1}}\right)$	
	$\gamma = \begin{cases} 1: \ 0<\frac{f_i-f_{i-1}}{f_{i+1}-f_{i-1}}<1 \\ 0: \ \text{otherwise} \end{cases}$	Δx^2 Δx
QUICK	$+\frac{3}{8}f_{i+1}+\frac{3}{4}f_i-\frac{1}{8}f_{i-1}$	Δx^3
CDS-4	$-\frac{1}{16}f_{i+2}+\frac{9}{16}f_{i+1}+\frac{9}{16}f_i-\frac{1}{16}f_{i-1}$	Δx^4

the nodes i and $i+1$ a parabola is used to approximate the function f. Three instead of two nodes must be taken into account in order to construct this polynomial. The third point is taken from the upstream side, which is in accordance with the nature of convection. By performing Taylor series expansions it can be shown that this quadratic interpolation has a third-order leading truncation error term. However, it is important to mention that the QUICK scheme is still of second-order accuracy if it is used in conjunction with the midpoint rule approximation of the surface integral (Equation 20). Although this restriction holds true for other higher order interpolations, the CDS-4 scheme was implemented which is the natural extension of CDS-2 and QUICK. It fits a third-order polynomial through four nodes. Two nodes are taken from the upstream side and two nodes from the downstream side. Similar to CDS-2, the CDS-4 scheme is a symmetric interpolation which does not depend on the flow direction, such as the HYBRID or the QUICK scheme. Again, in combination with the midpoint rule, this scheme formally has the same order of accuracy as CDS-2, QUICK and in most cases HLPA. However, despite this fact large differences will be observed in the quality of LES results if these different schemes are used for LES computations. This will demonstrate that the numerical dissipation produced by the scheme for the convective fluxes is of much greater relevance for LES than its formal order of accuracy in space itself. This topic will be discussed below.

It should also be mentioned that all viscous fluxes are approximated by central differences of second-order accuracy, which fits the elliptic nature of the viscous effects.

On non-staggered grids, as used in the present investigation, a special interpolation technique for the cell face velocities is necessary to avoid the decoupling of pressure and velocity components, leading to unphysical oscillations. These cell face velocities are needed to determine the mass fluxes at the cell faces. The momentum interpolation of Rhie and Chow [17] provides a proper coupling procedure. The influence of this approach on the solution was investigated in detail by Miller and Schmidt [18] and by Kobayashi and Pereira [19]. They

found that the momentum interpolation on non-staggered grids is nearly equivalent to the SIMPLE algorithm on staggered grids, with respect to formal error analysis and attained accuracy of the calculations.

5.2. Temporal discretization

Time advancement is performed by a predictor–corrector scheme. A low-storage multi-stage Runge–Kutta method (three substeps, second-order-accurate in time) is applied to integrate the momentum equations in the predictor step. Within the corrector step the Poisson equation for the pressure correction (SIMPLE method) is solved implicitly by the incomplete LU decomposition method of Stone [20] which is accelerated by a FAS multi-grid technique. Explicit time marching works well for LES with small time steps which are necessary to resolve turbulence motion in time. Due to the higher stability limit of the Runge–Kutta scheme, much larger time steps ($CFL = O(1)$) can be used than with the previously applied Adams–Bashforth scheme. This leads to a reduction in computing time by a factor of about two.

5.3. Performance and validation of the code

LESOCC is a highly vectorized computer code (vectorization rate $> 99.8\%$) because it was originally developed for high-performance mainframe computers such as CRAY, NEC or Fujitsu. Based on the shared memory architecture of the NEC SX-4 vector-parallel machine, it was recently parallelized on a microtasking level. Table II gives an overview of the sustained performance for a simulation with a fixed number of grid points (≈ 2 million) and a varying number of processors. With an increasing number of processors, the load (vector length) on each powerful vector-processor decreases, which results in a lower parallel efficiency. Nevertheless, this straightforward method of parallelization leads to a reasonable performance provided that the load per processor is large enough.

Before **LESOCC** was applied to the flow problem of the present investigation it was extensively tested and verified by LES computations of a variety of different test cases. This included plane channel flow, flows through a straight square duct and a 180° bend [9], flow around a surface mounted cubic obstacle placed in a plane channel [10–12] and flow past a long square cylinder [11,21]. In the course of this validation process both internal and external flows at low and high Reynolds numbers were successfully computed. Good agreement with other LES computations was demonstrated, especially at the Tegernsee workshop [1] and the ERCOFTAC workshop [2].

6. DETAILS OF THE TEST CASE

As described above, the flow past a long, circular cylinder is an appropriate test case for the intended investigations. First a low (subcritical) Reynolds number of 3900 (based on cylinder

Table II. Measurements of sustained performance on NEC SX-4

No. of processors	Sustained performance (Mflops s^{-1})	Speed-up	Parallel efficiency (%)
1	950	1.00	100.0
4	3699	3.89	97.3
8	6012	6.33	79.1

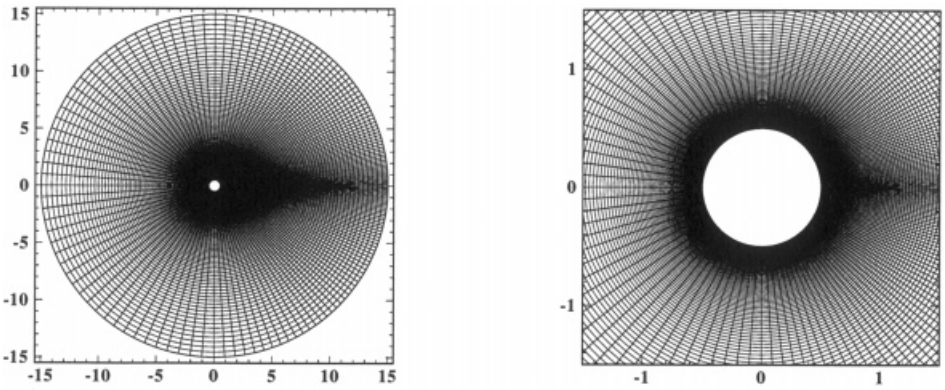

Figure 2. Cross-sectional grid (x–y-plane) and zoom of the near-wall region. Grid for Run **A**, **B1**–**5**, **C1**–**3** and **D1**–**3**.

diameter D and free-stream velocity u_∞) is chosen. It is known from experiments that transition takes place for this Reynolds number in the free shear layers. The flow problem has already been simulated and analyzed by Beaudan and Moin [22]. No-slip boundary conditions are used at solid walls for this low Reynolds number, whereas for high Reynolds number computations two different wall function approaches are available in **LESOCC** [9,10]. In the spanwise direction of the cylinder, periodicity of the flow is assumed. At the inflow plane constant velocity is imposed. The reason for adding no perturbations at the inlet section and therefore assuming a zero turbulence level is based on the following consideration. Even if the generation of turbulent fluctuations with appropriate length scales is possible, e.g. by an additional simulation of homogeneous, isotropic turbulence, the probability that these small perturbations imposed at the inlet will reach the cylinder is small. Because the grid is typically stretched from the cylinder surface to the outer boundaries (see Figure 2), the control volumes near the inlet are large. Therefore, all inflow fluctuations will be highly damped. Experience with the square cylinder test case [21] has shown that in general this inflow turbulence totally disappears until the flow reaches the cylinder.

A convective boundary condition given by

$$\frac{\partial u_i}{\partial t} + u_\infty \frac{\partial u_i}{\partial x} = 0, \tag{21}$$

is used at the outflow boundary. This condition ensures that vortices can approach and pass the outflow boundary without significant disturbances or reflections into the inner domain. In all previous LES computations of different test cases [9,10,21] the convective boundary condition was found to work very well. Likewise, no difficulties were observed in the case of the circular cylinder flow.

Various curvilinear, O-type grids were generated for this investigation. Table III gives an overview of these different grids, the corresponding number of control volumes and the size of the domain. All grids except one consist of 165×165 control volumes in the cross-sectional plane (see Figure 2). Primarily two grids were used in this study which only differ in the number of control volumes in the spanwise direction (32 for **B**/**C** and 64 for **D**). The size of the integration domain for these grids is $30D$ in the cross-section and πD in the direction of the cylinder axis. Additionally, three other version are used. The first (Run **A**) is for a 2D computation with only one control volume in the spanwise direction. The second (Run **E1**) is for a test with a larger domain in the spanwise direction, and the third (Run **E2**) covers a four

Table III. Overview of all simulations of the circular cylinder flow: parameters and computed integral quantities

Run	Grid	Domain	Scheme	SGS M.	L_r/D	C_d	$C_{P_{back}}$	Θ_1	Θ_2	Θ_3
A	$165\times165\times1$	$30D\times\pi D$	CDS-2	–	–	1.625	−2.008	100.7	138.2	–
B1	$165\times165\times32$	$30D\times\pi D$	HYBRID	Smago.	0.397	1.486	−1.665	95.2	126.0	–
B2	$165\times165\times32$	$30D\times\pi D$	HLPA	Smago.	0.630	1.319	−1.432	91.4	115.5	–
B3	$165\times165\times32$	$30D\times\pi D$	QUICK	Smago.	1.686	0.969	−0.867	86.7	121.5	150.6
B4	$165\times165\times32$	$30D\times\pi D$	CDS-2	Smago	1.115	1.099	−1.049	87.9	112.0	147.3
B5	$165\times165\times32$	$30D\times\pi D$	CDS-4	Smago.	1.214	1.071	−1.011	87.6	113.7	150.6
C1	$165\times165\times32$	$30D\times\pi D$	CDS-2	–	0.994	1.144	−1.115	88.6	111.3	150.6
C2 = B4	$165\times165\times32$	$30D\times\pi D$	CDS-2	Smago.	1.115	1.099	−1.049	87.9	112.0	147.3
C3	$165\times165\times32$	$30D\times\pi D$	CDS-2	Dynam.	1.197	1.071	−1.011	87.7	113.4	148.8
D1	$165\times165\times64$	$30D\times\pi D$	CDS-2	–	0.870	1.156	−1.164	89.3	116.7	–
D2	$165\times165\times64$	$30D\times\pi D$	CDS-2	Smago.	1.043	1.097	−1.069	88.5	119.0	–
D3	$165\times165\times64$	$30D\times\pi D$	CDS-2	Dynam.	1.372	1.016	−0.941	87.4	–	–
E1	$165\times165\times64$	$30D\times2\pi D$	CDS-2	Smago.	1.114	1.089	−1.036	87.9	113.2	146.2
E2	$209\times165\times32$	$120D\times\pi D$	CDS-2	Smago.	1.106	1.081	−1.023	88.0	112.7	148.9
Experiments [23–25]					1.33 ± 0.2	0.98 ± 0.05	-0.90 ± 0.05	85.0 ± 2.0	–	–

times larger domain in the cross-sectional plane. The internal region of this grid (radius $\leq 15D$) is identical to the other grids. The additional points in the radial direction are added to extend the grid to its new outer size. In all cases the grid points are clustered in the vicinity of the cylinder (geometrical series with a stretching factor of 1.03) and in the wake region.

In general, statistics were compiled over periods of at least $100D/u_\infty$ time units or ≈ 22 vortex shedding cycles. In most cases even longer periods of more than $200D/u_\infty$ time units were computed to prove convergence of the statistics. Of course, additional averaging was performed in the spanwise direction. Figure 3 impressively demonstrates why averaging must be done over such long time periods. Typical time histories of the computed lift coefficient C_l and drag coefficient C_d are plotted for a period of ≈ 140 vortex shedding cycles. Apart from cyclic oscillations due to the vortex shedding phenomenon and high-frequency turbulent fluctuations, the signals clearly have a low-frequency component which modulates the time history of C_l and C_d. In order to achieve reproducible statistics, this low-frequency modulation must be compensated by long averaging periods.

7. RESULTS AND DISCUSSION

7.1. Three-dimensional effects

In order to show the necessity for three-dimensional computations for LES, a 2D simulation was carried out in addition to 3D simulations. For the 2D case the same code and the same cross-sectional grid with only one control volume in the spanwise direction were used. Table III gives an overview of all simulations. For investigations on the impact of three-dimensionality, simulation **A** must be compared with Run **C1**. Both simulations were carried out with the CDS-2 scheme and no subgrid scale model. Figure 5 shows the streamlines of the time-averaged flow field. Totally different streamline patterns can be observed for the 2D (**A**) and the 3D simulations (**C1**). The largest difference is given by the absence of an attached recirculation region behind the cylinder in the 2D case. Despite the similar averaging time for the 2D and 3D simulations, the 2D flow field is more asymmetric than the 3D flow field. Even increasing

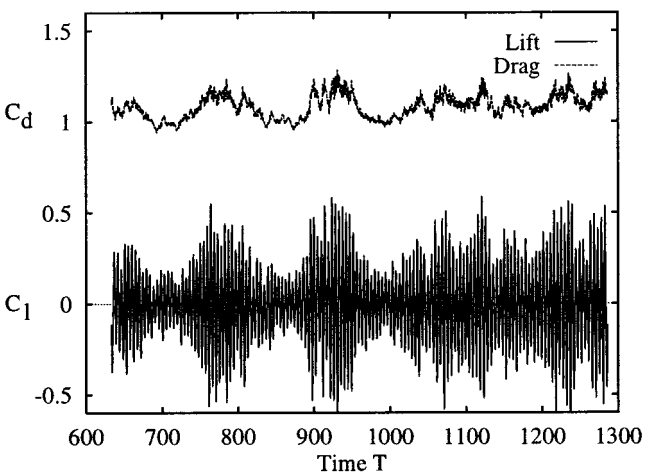

Figure 3. Typical time history of the lift coefficient C_l and the drag coefficient C_d for the flow past a circular cylinder, $Re = 3900$ (≈ 140 vortex shedding cycles).

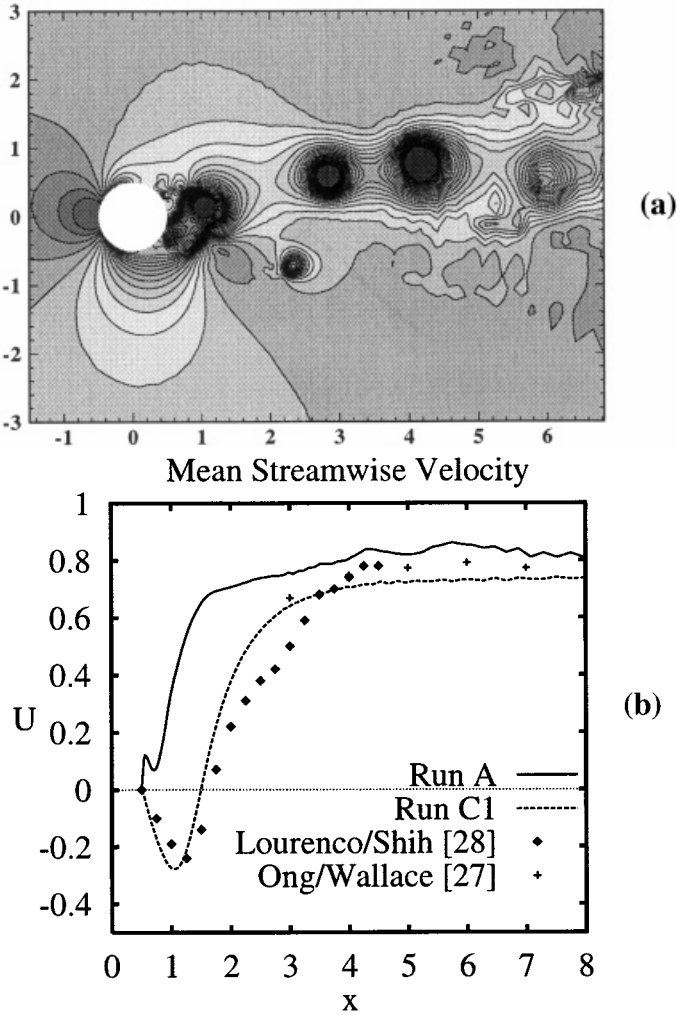

Figure 4. (a) Instantaneous pressure distribution for the flow past a circular cylinder, $Re = 3900$, 2D LES (Run **A**). (b) Comparison of the mean streamwise velocity along the centerline for a 2D LES (Run **A**) and 3D LES (Run **C1**).

the averaging time does not improve the 2D results significantly. The reason for this strange behavior can only be detected by observations of the instantaneous flow structure past the cylinder. In contrast to the 3D LES, asymmetric vortex shedding with a non-zero mean lift coefficient is observed in the 2D case. This phenomenon is shown in Figure 4(a) by a plot of the instantaneous pressure distribution. The vortices which shed from the cylinder move downstream along an axis which is inclined with reference to the symmetry line. Irregularly, the axis of the vortex street changes from positive to negative angles and the other way round. Similar observations have been reported [26]. Owing to this behavior, the asymmetric time-averaged streamlines can be explained.

In contrast to experimental measurements by Lourenco and Shih [28] and Ong and Wallace [27] and the results of the 3D LES, the 2D simulation shows an (unphysical) positive time-averaged streamwise velocity distribution at all centerline stations downstream of the cylinder (Figure 4(b)). In the 3D case (**C1**), the flow field consists of a large recirculation

region behind the cylinder and two additional, small separation bubbles attached to the downstream face of the cylinder. As a result of this flow structure the computed drag coefficient C_d and the back-pressure coefficient $C_{P_{back}}$ are much too high in the 2D case compared with experimental measurements (e.g. Norberg [24]: $C_d = 0.98 \pm 0.05$ and $C_{P_{back}} = -0.9 \pm 0.05$). The large deviations between the 2D and 3D results indicate that three-dimensional structures strongly influence the near-wake of the flow. Beaudan and Moin [22] have already pointed out that these structures consist of pairs of counter-rotating streamwise vortices, which cannot be captured by a 2D calculation. This is an illustrative proof that 2D LES (as well as DNS) is useless, owing to the impact of three-dimensionality of the flow even in case of (nearly) two-dimensional flow problems.

7.2. Influence of discretization scheme

The second aspect investigated is the influence of different approximations for the convective fluxes in the filtered Navier–Stokes equations. For this purpose, five different simulations (Runs **B1**–**5**, see Table III) were carried out which differed only according to this detail. All simulations were based on the grid with $165 \times 165 \times 32$ control volumes and the Smagorinsky model with $C_s = 0.1$. Figure 5 shows a first qualitative comparison of the time-averaged streamlines. Although it is already known in the LES community that the discretization scheme plays a dominant role for the quality of the solution, it is worth demonstrating this important issue by illustrative applications. As shown in Figure 5, the structure and the length of the recirculation bubbles behind the cylinder are strongly influenced by the numerical scheme. A recirculation region behind the cylinder exists in all simulations. Additionally, two small counter-rotating vortices attached to the backward side of the cylinder can be observed. Therefore, three angles can be determined: the primary separation angle Θ_1, the reattachment angle Θ_2 and the secondary separation angle Θ_3. The values are listed in Table III in conjunction with the recirculation length L_r/D, the drag coefficient C_d and the back-pressure coefficient $C_{P_{back}}$. The Strouhal number of the vortex shedding frequency has not been included in Table III because the computed values for all simulations are found to be within the experimental range of $St = 0.215 \pm 0.005$, determined by Cardell [25]. Apparently, this quantity is not very sensitive to the parameters of the simulation. Rodi *et al.* [1] have already pointed out that accurate prediction of the Strouhal number is not necessarily an indication of a quality simulation.

As known from measurements (e.g. Reference [23]), separation should take place before the apex of the cylinder at $\approx \Theta_1 = 85 \pm 2$. In Run **B1** (HYBRID scheme) separation is postponed for $\approx 10^o$. The recirculation length is only one third of the experimental value, resulting in a much too high back-pressure coefficient and drag value. Simulation **B2** shows a similar trend. However, the results are slightly better quantitatively but still not in good agreement with the measured values. Run **B3**, based on the QUICK scheme, shows an opposite behavior. Here the computed recirculation length is $\approx 27\%$ larger than the experimental value and the back-pressure and drag coefficients are even smaller than in experiments. This is a totally unexpected result. As already mentioned above, the QUICK scheme combined with the midpoint rule is of second-order accuracy. It generates a disperse third-order error term and also a dissipative fourth-order error term that acts like an additional subgrid scale model. Similarly to the dissipative second-order error term of the HYBRID and the HLPA schemes, the fourth-order term is expected to add numerical diffusion to the problem leading, at least in part, to shorter recirculation zones. The QUICK scheme, however, shows the opposite result and no explanation can be offered for this behavior. Based on experiences with much simpler test cases (e.g.

plane channel flow and square duct flow [9,10]) which allow investigations on grids with strongly varying resolutions, no significant improvements of the LES results for the circular cylinder flow are expected for the QUICK scheme on finer grids.

The best results compared with experiments (e.g. Reference [27]) are achieved by the CDS-2 and CDS-4 schemes. The error terms of both schemes do not have any even component (second- or fourth-order derivatives) which damp out high-frequency components in the solution. The results of CDS-4 (**B5**) are in slightly better agreement with experimental observation than those of CDS-2 (**B4**). However, the variations between these two results are much smaller than among the others. In Figure 6 the time-averaged streamwise velocity distribution (U) along the centerline is plotted in comparison with measurements by Lourenco and Shih [28] and Ong and Wallace [27].

This figure summarizes the observations based on the streamline plots. Additionally, the distribution of the resolved turbulent kinetic energy k is shown. The HYBRID scheme (**B1**)

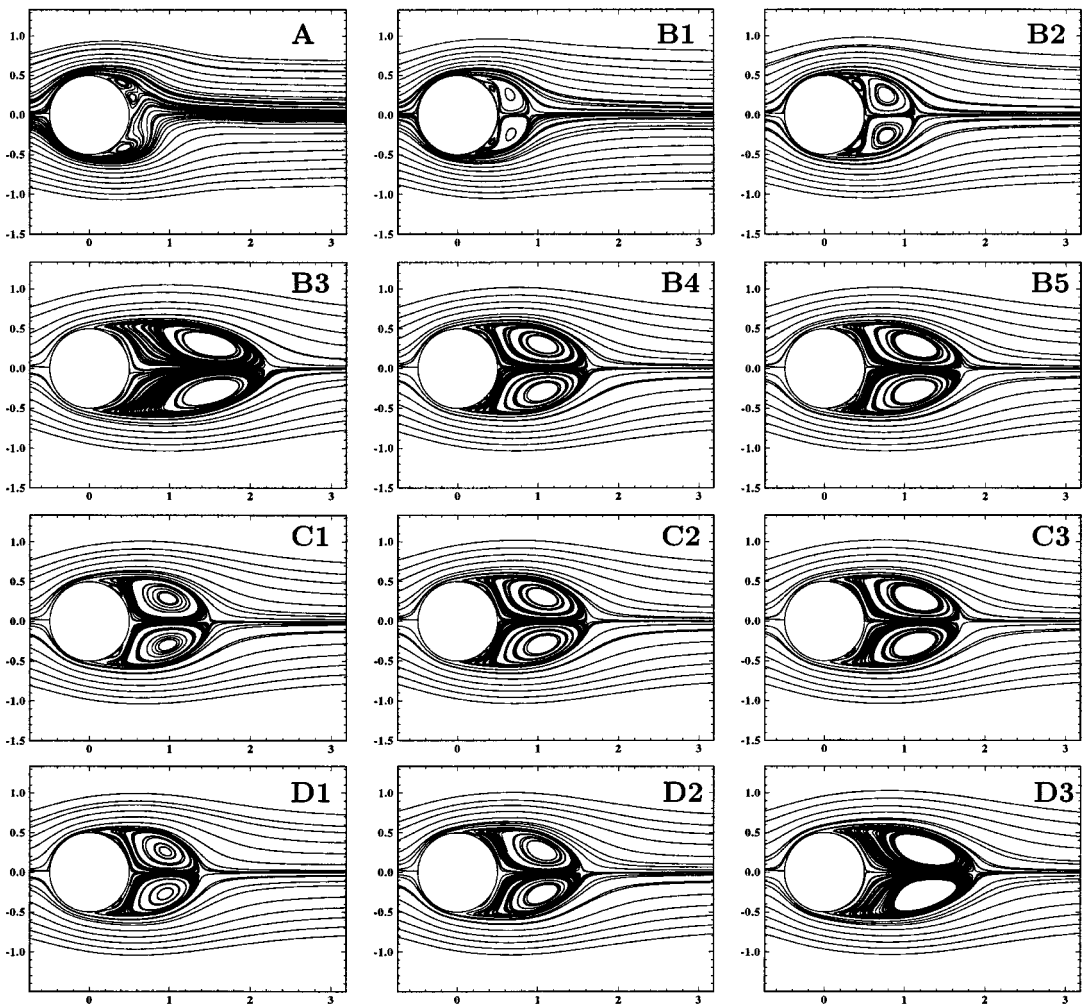

Figure 5. Time-averaged streamlines in the x–y-plane for the flow past a circular cylinder, $Re = 3900$ (for legend see Table III).

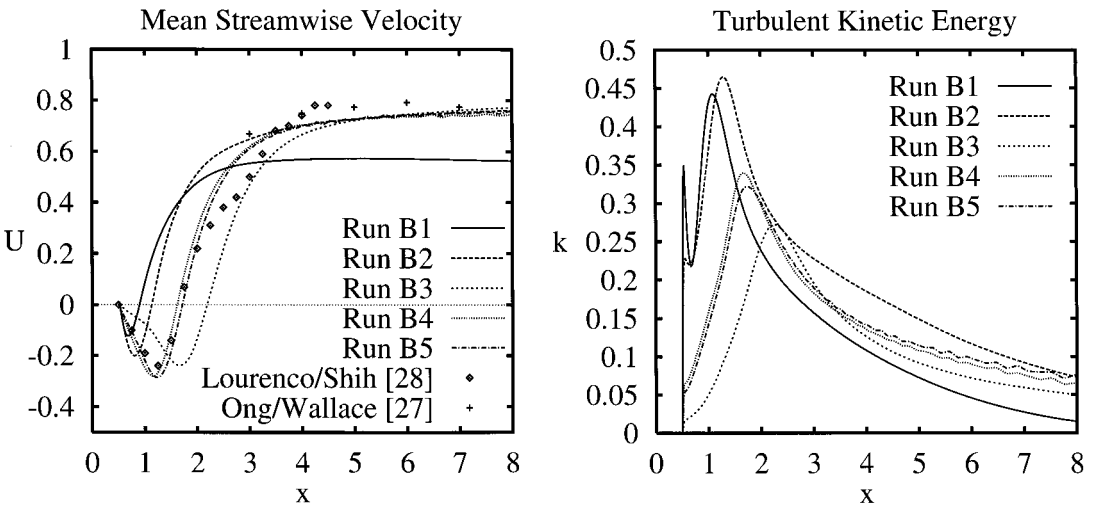

Figure 6. Mean streamwise velocity and total resolved turbulent kinetic energy along the centerline for Runs **B1**–**5**.

and the HLPA scheme (**B2**) generate the largest maxima of k close to the cylinder in a distance of $\approx 0.5D$ and $0.75D$, respectively. Additional peaks of k can be observed directly in the vicinity of the wall. The maxima of k produced by CDS-2 (**B4**) and CDS-4 (**B5**) are smaller than for **B1** and **B2** and their locations further downstream. The lowest maximum is achieved by the QUICK scheme (**B3**). In all simulations the position of the maxima coincides fairly well with the recirculation length L_r/D. The high levels of k, however, especially for **B1** and **B2** must be explained because they seem to be contradictory to the high numerical diffusion produced by these approximations. In the circular cylinder flow there is strong vortex shedding behind the cylinder, accompanied by turbulent fluctuations. Owing to this large scale vortex shedding the resolved turbulent kinetic energy k is a sum of the quasi-periodic oscillations and the resolved turbulent fluctuations. In order to separate these two effects it would be necessary to perform phase-averaging, which is associated with several problems as described by Breuer and Pourquié [21]. Looking at instantaneous flow fields of **B1**–**5**, however, the apparent contradiction turns out fine. Figure 7 shows the distribution of the instantaneous spanwise vorticity component ω_z in a cross-sectional plane for Runs **B1**–**4**. Simulation **B5** is omitted here because it is very similar to **B4**. It should be mentioned that Figure 7 does not show the same phase of the vortex shedding cycle for the different simulations. Nevertheless, in cases **B1** and **B2** the simulated flow looks like laminar vortex shedding, showing almost no turbulent fluctuations, as expected for LES of a turbulent flow. This means that the high levels of k for these simulations are almost completely generated by the quasi-periodic vortex shedding and not by turbulent fluctuations. This observation is consistent with the high level of numerical diffusion typical for upwind schemes (**B1**–**2**). Simulations **B4** and **B5** generate instantaneous flow fields as expected for the flow past a cylinder at a subcritical Reynolds number. The vortex shedding motion is superimposed by strong turbulent fluctuations. Again, the result of Run **B3** is difficult to explain. Turbulent motions can be observed. However, exact splitting of quasi-periodic and turbulent components cannot be achieved without phase-averaging.

7.3. Influence of subgrid scale modeling

In comparison with the large variations of the results of applying different numerical schemes, Figure 5 indicates a small influence of subgrid scale modeling (Runs **C1**–**3**). This is

a series of three simulations in which only the model for the non-resolvable subgrid scale stresses was varied. The computed integral quantities are listed in Table III. Simulation **C1** without any subgrid scale model shows the shortest recirculation length and the highest back-pressure and drag coefficient of all **C** cases. Applying the Smagorinsky model (**C2**) results in slightly improved values. The recirculation length increases and accordingly the drag decreases. This trend continues if the dynamic model (**C3**) is applied instead of the Smagorinsky model. The distribution of the pressure coefficient C_p and the friction coefficient C_f on the surface of the cylinder is plotted in Figure 8 for **C1**–**3**. In the front part of the cylinder almost no differences in the results can be observed. The flow is laminar in this region, therefore, subgrid scale modeling does not have any influence (as expected). Small deviations occur on the backward side, however, particularly for the pressure distribution. The results obtained with the Smagorinsky (**C2**) and dynamic models (**C3**) are close to each other and show better agreement with experimental values for $Re = 3000$ [24] than **C1** without any subgrid scale model. The size of the separation and reattachment regions on the cylinder is similar in all simulations.

In Figure 9 the time-averaged streamwise velocity U and the resolved turbulent kinetic energy k along the centerline are plotted for Runs **C1**–**3**. As observed before, the location of the maximum of k corresponds fairly well with the recirculation length. It appears that k is reduced when the Smagorinsky model is applied. Surprisingly, k is further reduced when the Smagorinsky model is replaced by the dynamic approach.

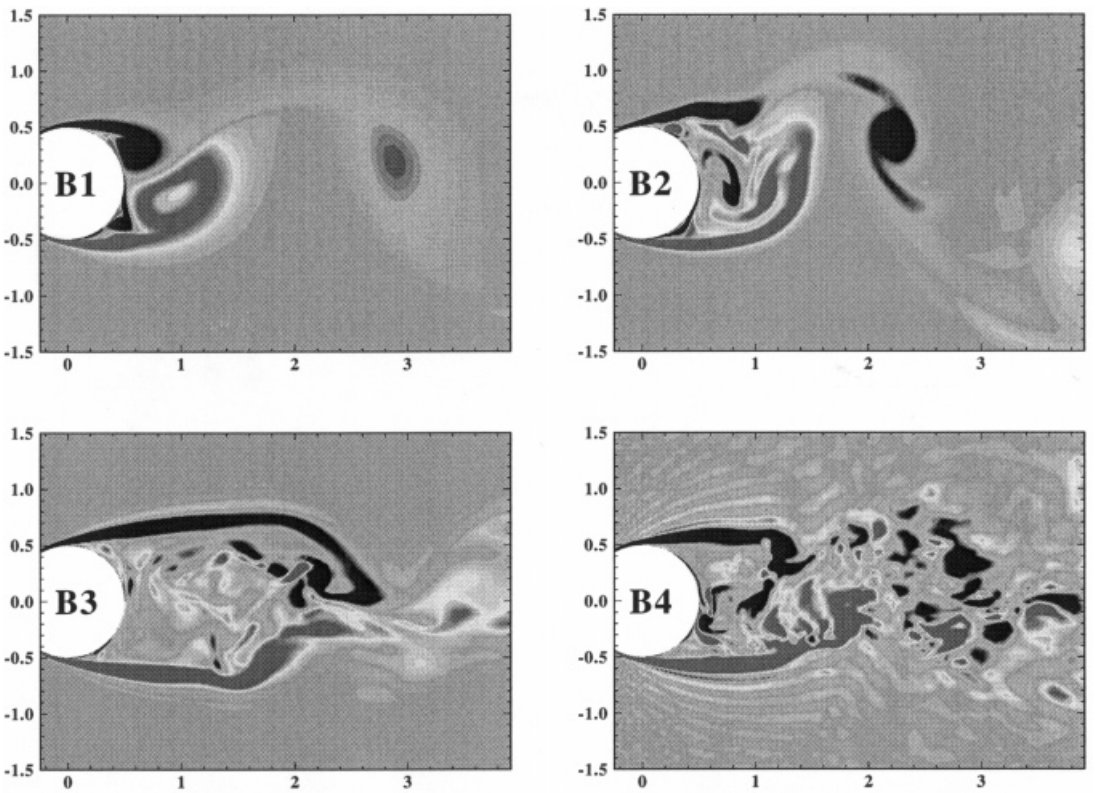

Figure 7. Distribution of the instantaneous vorticity component ω_z in a cross-sectional plane (x–y-plane) for Runs **B1**–**4**.

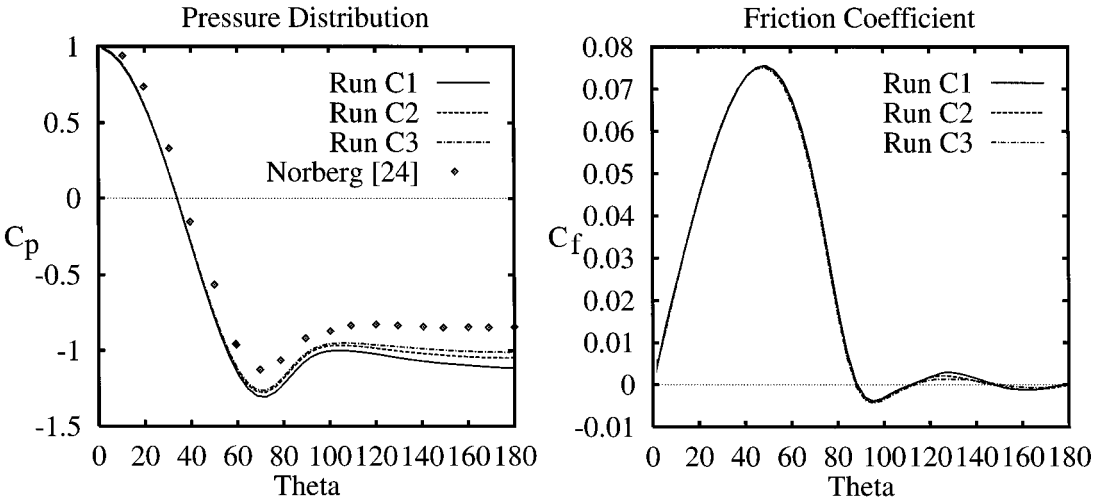

Figure 8. Pressure coefficient C_p and friction coefficient C_f on the surface of the cylinder using different subgrid scale models (Runs **C1**–**3**).

7.4. Influence of resolution

In order to investigate the influence of the spanwise resolution, a new series of simulations **D1**–**3** has been carried out which differs from **C1**–**3** only by the doubled number of control volumes in the spanwise direction. Again, Figure 5 shows the streamline plots of the time-averaged flow and Table III lists the computed integral parameters. The largest deviation between a **D** and a corresponding **C** result occurs for the simulation applying the dynamic model (**C3**/**D3**). In Figure 10 the distribution of the pressure coefficient C_p and the friction coefficient C_f on the surface of the cylinder is plotted for Runs **D1**–**3**. The corresponding results of Runs **C1**–**3** are shown in Figure 8. Surprisingly, the deviations between the results achieved by different subgrid scale models increase with increasing resolution in the spanwise direction. In comparison with the experimental measurements of Norberg [24], only the results of the

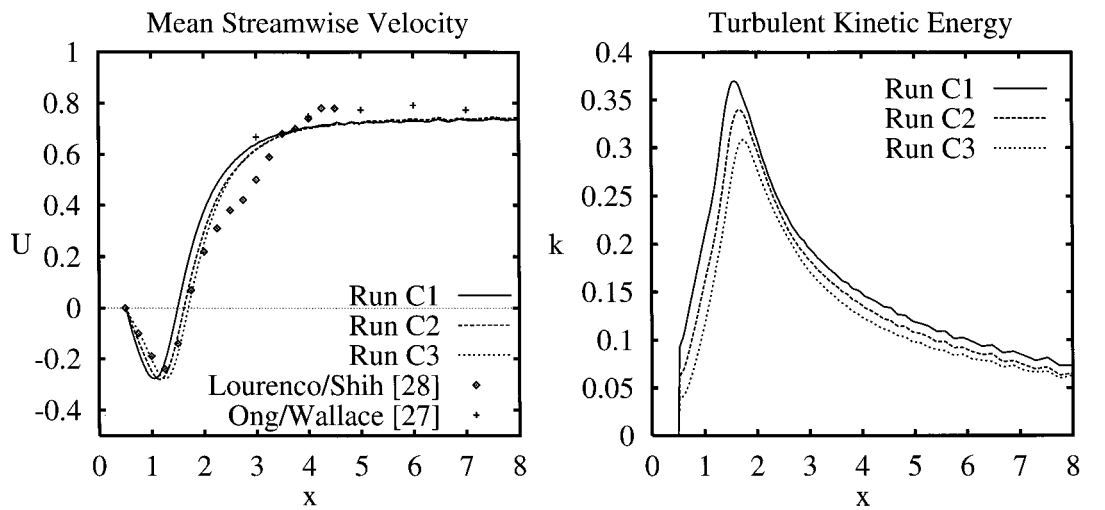

Figure 9. Mean streamwise velocity and total resolved turbulent kinetic energy along the centerline for Runs **C1**–**3**.

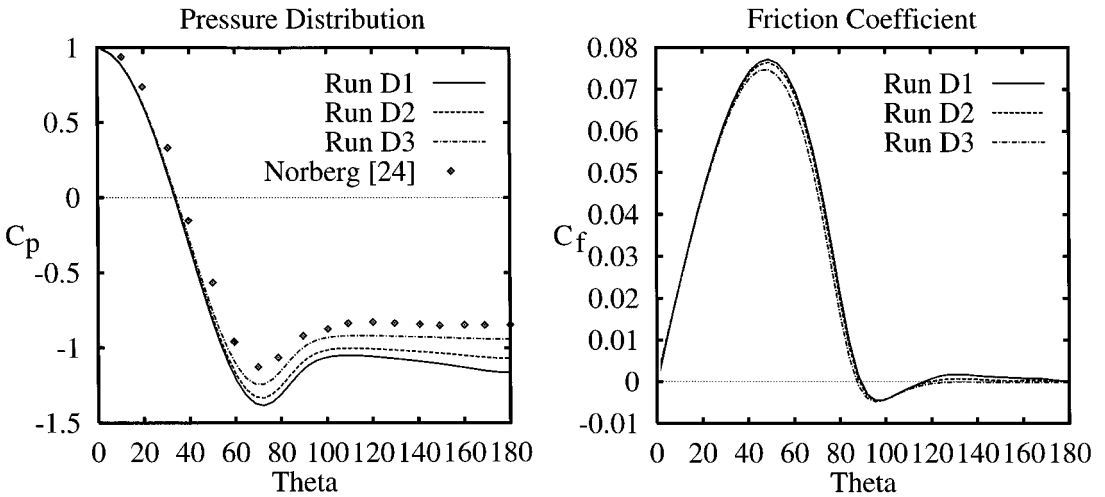

Figure 10. Pressure coefficient C_p and friction coefficient C_f on the surface of the cylinder using different subgrid scale models (Runs **D1**–**3**).

dynamic model (**D3**) are improved by grid refinement. Run **D3** shows a fairly good agreement with the measurements and with the integral quantities listed in Table III. In the case of no model (**D1**) or Smagorinsky model (**D2**) the agreement with experiment even becomes worse by spanwise refinement. An interesting effect can be observed in the plot of the friction coefficient C_f. In contrast to Run **C3**, simulation **D3** shows no reattachment on the backward side of the cylinder. Therefore, the reattachment angle Θ_2 and the secondary separation angle Θ_3 could not be given in Table III. As shown in Figure 5, the small counter-rotating vortices attached to the backward side of the cylinder totally disappear in this case. However, from the experimental point of view it is not clear whether these weak vortices exist at all.

In Figure 11 the time-averaged streamwise velocity U and the turbulent kinetic energy k are plotted along the centerline for Runs **D1**–**3**. In comparison with the results of series **C** in Figure 9, a similar trend as in the C_p and C_f plots can be observed. The deviations between the results achieved with different models do not decrease on improving the spanwise resolution. For both quantities (U and k) the deviations are even emphasized. Furthermore, it is important to note that the turbulent kinetic energy k increases for all subgrid scale models when the number of control volumes is doubled in the spanwise direction.

Figures 12 and 13 show total Reynolds stress profiles in the near wake ($x/D = 1.54$), obtained from Runs **C1**–**3** and **D1**–**3**, respectively. The streamwise Reynolds stress $u'u'$ is quite well predicted for all simulations in comparison with measurements by Lourenco and Shih [28]. The dynamic model (**C3**/**D3**) yields slightly better results. However, the cross-stream Reynolds stress $v'v'$ is highly overpredicted in the simulation without any subgrid scale model (**C1**/**D1**) and with the Smagorinsky model (**C2**/**D2**). This result is totally contradictory to the observations of Beaudan and Moin [22], who found underpredicted values of this quantity when applying no subgrid scale model or the Smagorinsky model. Again, the dynamic model (**D3**) shows quite good agreement with the measurements in accordance with the simulations of Beaudan and Moin [22]. Comparing the results obtained on grids with different numbers of control volumes in the spanwise direction yields the same trend as observed for the other quantities discussed before. Spanwise grid refinement leads to increased deviations between the results computed with different subgrid scale models. In general, only the results achieved by application of the dynamic model are improved by finer grids in the spanwise direction.

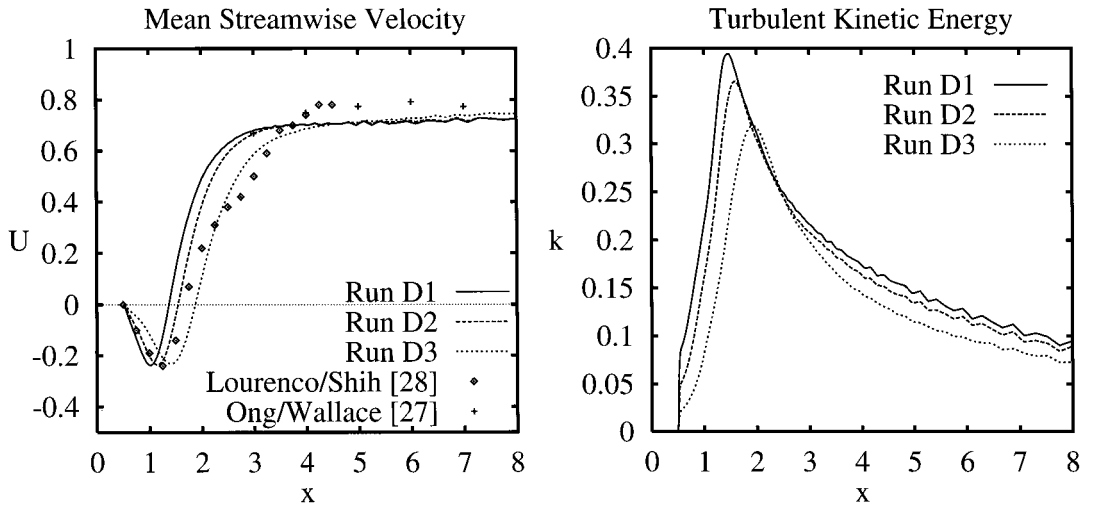

Figure 11. Mean streamwise velocity and total resolved turbulent kinetic energy along the centerline for Runs **D1**–**3**.

Finally, two more aspects were investigated. First the domain of integration is doubled in the spanwise direction (Run **E1**) by doubling the number of grid points compared with **C2** while keeping the spanwise cell size constant. According to the computed integral parameters, this modification does not improve the results significantly. Another test (Run **E2**) increases the domain of integration four times in the radial direction, while keeping the internal grid unchanged (as described above). In addition, this modification is rather irrelevant to the computed results, indicating that the previously used domain size is sufficient.

8. CONCLUSIONS

The flow past a circular cylinder at a subcritical Reynolds number of $Re = 3900$ was simulated by the method of LES. The finite volume code (**LESOCC**) employed was written for general

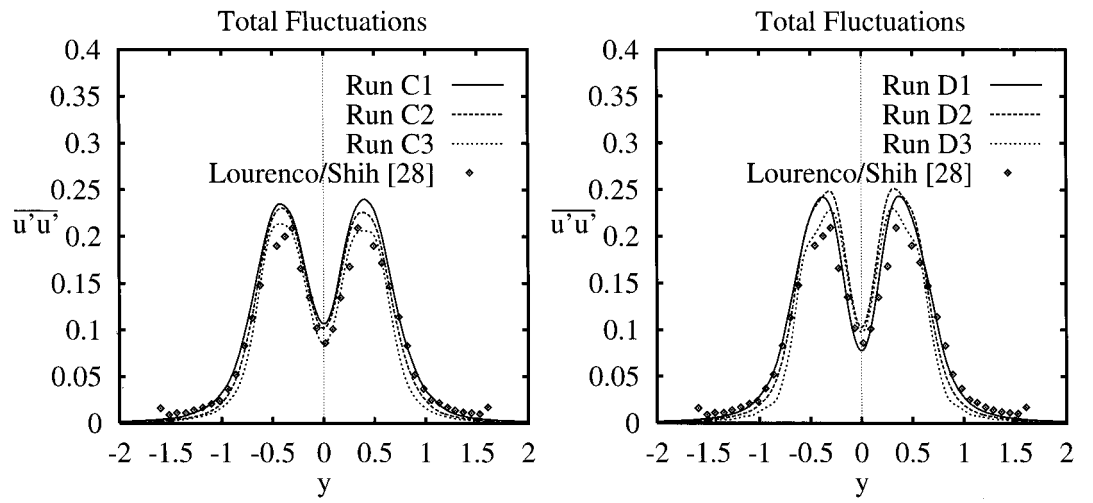

Figure 12. Total resolved Reynolds stresses $\overline{u'u'}$ at $x/D = 1.54$ for Runs **C1**–**3** and **D1**–**3**.

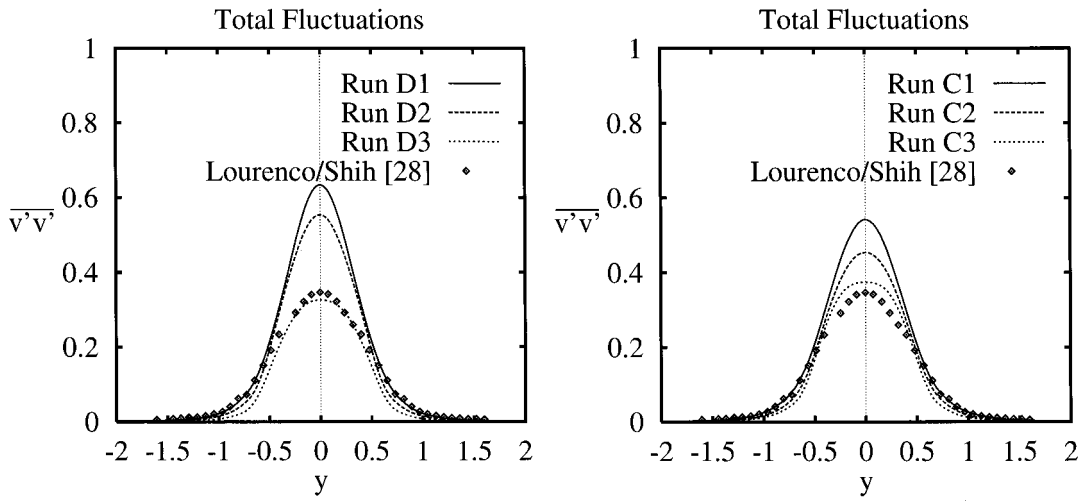

Figure 13. Total resolved Reynolds stresses $\overline{v'v'}$ at $x/D = 1.54$ for Runs **C1–3** and **D1–3**.

curvilinear grids in order to permit the computation of practically relevant flows in or around complex geometries. The recently proposed dynamic subgrid scale model was applied in addition to the Smagorinsky model. Additionally, simulations without any SGS model were carried out. The objective of the present work was not to study the physics of the flow past circular cylinders in detail but to carry out an extensive investigation on numerical and modeling aspects influencing the quality of LES solutions. The strong impact of three-dimensionality for LES calculations and the important aspect of low-diffusive discretization schemes for convective fluxes have been presented and discussed. The investigation confirmed the statement that the numerical dissipation produced by a scheme is more crucial for LES than its formal order of accuracy. Central schemes of second- (CDS-2) or fourth-order accuracy (CDS-4) in space turned out to be well suited for LES, whereas upwind schemes even of higher order accuracy cannot be recommended for such simulations. Furthermore, the influence of subgrid scale modeling and spanwise resolution has been studied in detail. Drawing conclusions from the investigations above, the dynamic model (**D3**) combined with central differencing (CDS-2) yields the best solution, which agrees quite well with experimental measurements. Finally, the important role of spanwise resolution, which has often been underestimated for LES of flow problems with one homogeneous direction, must be emphasized.

ACKNOWLEDGMENTS

Financial support by the Bayerische Forschungsstiftung in the Bavarian Consortium of High-Performance Scientific Computing (FORTWIHR II) is gratefully acknowledged. The simulations were mainly carried out on the NEC SX-4 machine of the High-Performance Computing Center, Stuttgart. This support is also gratefully acknowledged.

REFERENCES

1. W. Rodi, J.H. Ferziger, M. Breuer and M. Pourquié, 'Status of large eddy simulation: results of a workshop', Workshop on LES of Flows Past Bluff Bodies, Rottach-Egern, Tegernsee, Germany, June 26–28, 1995', *J. Fluids Eng.*, **119**, 248–262 (1997).
2. P.R. Voke, 'Flow past a square cylinder: test case LES2', *Proc. ERCOFTAC Workshop on Direct and Large Eddy Simulation*, Grenoble, France, September 16–19, 1996, ERCOFTAC Series **5**, 355–373 (1996), Direct and

Large-Eddy Simulation II, J.P. Chollet, P.R Voke and L. Kleiser (eds.), Kluwer Academic Publishers, Dordrecht, 1997.
3. C.H.K. Williamson, 'Vortex dynamics in the cylinder wake', *Annu. Rev. Fluid Mech.*, **28**, 477–539 (1996).
4. R.S. Rogallo and P. Moin, 'Numerical simulation of turbulent flows', *Annu. Rev. Fluid Mech.*, **16**, 99–137 (1984).
5. J. Smagorinsky, 'General circulation experiments with the primitive equations, I, the basic experiment', *Mon. Weather Rev.* **91**, 99–165 (1963).
6. M. Germano, U. Piomelli, P. Moin and W.H. Cabot, 'A dynamic subgrid scale eddy viscosity model', *Phys. Fluids A*, **3**, 1760–1765 (1991).
7. J. Bardina, J.H. Ferziger and W.C. Reynolds, 'Improved subgrid models for large eddy simulation', *AIAA Paper 80-1357* (1980).
8. D.K. Lilly, 'A proposed modification of the Germano subgrid scale closure method', *Phys. Fluids A*, **4**, 633–635 (1992).
9. M. Breuer and W. Rodi, 'Large eddy simulation of turbulent flow through a straight square duct and a 180° bend', *Fluid Mech. Appl.*, **26**, 273–285, Direct and Large Eddy Simulation I, Selected papers from the First ERCOFTAC Workshop on DNS and LES, Guildford, Surrey, UK, 27–30 March, 1994, P.R. Voke, L. Kleiser and J.P. Chollet (eds.), Kluwer Academic Publishers, Dordrecht, 1994.
10. M. Breuer and W. Rodi, 'Large-eddy simulation of complex turbulent flows of practical interest', *Flow Simulation with High-Performance Computers II*, E.H. Hirschel (ed.), Notes on Numerical Fluid Mechanics, **52**, 258–274, Vieweg Verlag, Braunschweig (1996).
11. M. Breuer, M. Pourquié and W. Rodi, 'Large-eddy simulation of internal and external flows', *3rd Int. Congress on Industrial and Applied Mathematics*, Hamburg, 3–7 July, 1995, in E. Kreuzer and O. Mahrenholtz (eds.), Spec. Issue of ZAMM, Issue 4: Applied Sciences—Especially Mechanics (Minisymp.), Akademie Verlag, Berlin, 1996, pp. 235–238.
12. M. Breuer, D. Lakehal and W. Rodi, 'Flow around a surface mounted cubical obstacle: comparison of LES and RANS—results', *IMACS-COST Conf. on CFD, 3-D Complex Flows*, Lausanne, Switzerland, September 13–15, 1995, In M. Deville, S. Gavrilakis and I.L. Rhyming (eds.), Computation of 3D Complex Flows, Notes on Numerical Fluid Mechanics, vol. 53, Vieweg Verlag, Braunschweig, 1996, pp. 22–30.
13. M. Breuer, 'Numerical and modeling influences on large eddy simulations for the flow past a circular cylinder', in *Proc. 11th Symposium on Turbulent Shear Flows*, vol. 3, 26:7–26:12, Grenoble, France, September 8–11, 1997.
14. M. Breuer, 'Large eddy simulation of the flow past bluff bodies: numerical and modeling aspects', in *Proc. Workshop on DNS and LES of Complex Flows, Numerical and Modeling Aspects*, 14–21, University of Twente, Twente, The Netherlands, July 9–11, 1997.
15. J. Zhu, 'A low-diffusive and oscillation-free convection scheme', *Commun. Appl. Numer. Methods*, **7**, 225–232 (1991).
16. B.P. Leonard, 'A stable and accurate convection modeling procedure based on quadratic upstream interpolation', *Comput. Methods Appl. Mech. Eng.*, **19**, 59–98 (1979).
17. C.M. Rhie and W.L. Chow, 'A numerical study of the turbulent flow past an isolated airfoil with trailing edge separation', *AIAA J.*, **21**, 1225–1532 (1983).
18. T.F. Miller and F.W. Schmidt, 'Use of pressure-weighted interpolation method for the solution of the incompressible Navier–Stokes equations on a non-staggered grid system', *Numer. Heat Trans.*, **14**, 213–233 (1988).
19. M.H. Kobayashi and J.C.F. Pereira, 'Numerical comparison of momentum interpolation methods and pressure-velocity algorithms using non-staggered grids', *Commun. Appl. Numer. Methods*, **7**, 173–186 (1991).
20. H.L. Stone, 'Iterative solution of implicit approximations of multidimensional partial differential equations', *SIAM J. Numer. Anal.*, **5**, 530–558 (1968).
21. M. Breuer and M. Pourquié, 'First experiences with LES of flows past bluff bodies', *Proc. 3rd Intern. Symp. of Engineering Turbulence Modeling and Measurements*, Heraklion, Crete, Greece, May 27–29, 1996, in W. Rodi and G. Bergeles (eds.), Engineering Turbulence Modeling and Exp., vol. 3, Elsevier Science, Amsterdam, 1996, pp. 177–186.
22. P. Beaudan and P. Moin, 'Numerical experiments on the flow past a circular cylinder at a sub-critical Reynolds number', *Report No. TF-62*, Thermosciences Division, Department of Mech. Engineering, Stanford University, 1994.
23. J. Son and T.J. Hanratty, 'Velocity gradients at the wall for flow around a cylinder at Reynolds numbers from 5×10^3 to 10^5', *J. Fluid Mech.*, **35**, 353–368 (1969).
24. C. Norberg, 'Effects of Reynolds number and low-intensity free stream turbulence on the flow around a circular cylinder', *Publ. No. 87/2*, Department of Applied Thermoscience and Fluid Mech., Chalmers University of Technology, Gothenburg, Sweden, 1987.
25. G.S. Cardell, 'Flow past a circular cylinder with a permeable splitter plate', *Ph.D. Thesis*, Graduate Aeronautical Lab., California Inst. of Technology (1993).
26. M. Meinke, 'Numerische Lösung der Navier–Stokes-Gleichungen für instationäre Strömungen mit Hilfe der Mehrgittermethode', *Ph.D. Thesis*, Aerodynamisches Institut, RWTH Aachen (1993).
27. L. Ong and J. Wallace, 'The velocity field of the turbulent very near wake of a circular cylinder', *Exp. Fluids*, **20**, 441–453, Springer Verlag, Berlin (1996).
28. L.M. Lourenco and C. Shih, 'Characteristics of the plane turbulent near wake of a circular cylinder, a particle image velocimetry study', Private Communication, 1993 (data taken from Reference [22]).

